



One-step PDA coating strategy on pure Zn for blood-contacting engineering

Xiaoyun Qi¹, Shicheng Zhou¹, Hui Fang¹, Shuhan Yang, Chunjin Hang, Yanhong Tian, Chenxi Wang*

State Key Laboratory of Advanced Welding and Joining, Harbin Institute of Technology, Harbin 150001, China



ARTICLE INFO

Article history:

Received 18 October 2021

Revised 13 December 2021

Accepted 21 December 2021

Available online 27 March 2022

Keywords:

Biodegradable

Pure Zn

Uniform corrosion

Blood compatibility

Doubled-coated structure

ABSTRACT

The mechanical performance degradation caused by pitting corrosion and the insufficient biocompatibility induced with ion release inhibit the application of Zn as the new biodegradable metallic materials for blood-contacting intervention therapy. This work successfully coats a uniform polydopamine (PDA) layer on pure Zn via a one-step deposition process without introducing heavy metal elements or detrimental additives. Enhanced corrosion resistance and uniform corrosion have been performed on PDA coated Zn with corrosion products and pits reduced significantly than pure Zn during *in vitro* degradation. Thrombosis could be prohibited by anticoagulation performance with prothrombin time and activated partial thromboplastin time prolonged after co-incubation, and an almost 40% decrease of platelets adhesion, indicating the improved blood compatibility of coated Zn. Additionally, the poly (lactic-co-glycolic acid) (PLGA) is filmed on PDA coated Zn to realize a smooth double-coated structure with superior mechanical performance under stress loading to stably serve the multifunctional application, such as drug loading. Our strategy not only represents a facile and biological friendly method for Zn surface modification but also puts forward new ideas on preparing PDA-based coatings on active biodegradable alloys, which are beneficial for better blood-contacting engineering.

© 2022 Published by Elsevier Ltd on behalf of The editorial office of Journal of Materials Science & Technology.

1. Introduction

Intervention therapy has attracted considerable attention as an effective method for treating coronary heart disease and myocardial infarction among clinics in recent years. Biodegradable metals deem to be promising candidates for the expected therapy procedure, which can make stents fully absorbed after curing patients, serving as an accurate and efficient treatment with comprehensive indications and fewer complications in a blood-contacting condition. To date, researchers have been studying the various biodegradable metallic materials and their performance from Fe alloy to Mg alloy [1–4]. Nevertheless, Fe stents with plastic deformation capacity lack optimal degradation rates [5–10], while Mg-based stents can be degraded too rapidly to maintain mechanical integrity before the cardiovascular function has been completely rebuilt [11–15].

As a relatively new biodegradable metal, Zn owns the superior corrosion rate according to its standard electrode potential between Fe and Mg [16]. It also acts as an essential trace element in the human body to effectively boost growth and maintain immune function [17]. In addition, the pure Zn degrades in a slow first and then fast mode in line with the requirement of blood-contacting devices for serving *in vivo* [18,19]. With mentioned properties, this material owns enormous potential in vascular stents and bone implants [18,20–22]. Unfortunately, several fatal defects were exposed when Zn acted as a foreign body for humoral contact investigation. The bare zinc and its alloy will be pitting corroded and release metal ions during service uncontrollably [23,24]. Corrosion pits induced non-uniform corrosion weakens the mechanical performance of the matrix and makes Zn vulnerable to fracture unpredictably under stress loading [25,26]. Meanwhile, platelets activities such as adhesion and migration are sensitive to loosed corrosion products [23,27,28]. Additionally, human aortic smooth muscle cells (AoSMC) and human aortic endothelial cells (HAEC) will change their life activity during the uncontrolled release of Zn ions, bringing about the risk of restenosis [29]. If the combination of promising degradation mode, stable mechanical properties, and excellent biocompatibility of Zn can be realized via surface modifica-

* Corresponding author.

E-mail address: wangchenxi@hit.edu.cn (C.-X. Wang).

¹ These authors contributed equally to this work.

tion, it will bring more possibilities to overcome the bottleneck of Zn in blood-contacting engineering.

The combination of biodegradable alloys and coatings, such as poly (lactic-co-glycolic acid) (PLGA), hydroxyapatite, and collagen, is widely accepted as an available solution to modernize the metal surface for biocompatibility promotion and drug loading, and so on [30–32]. Besides, multilayer or co-coated film structures are required in clinics for multifunctional treating, which should possess sufficient mechanical capability under stress loading for stably serving in the human body. Mussel-inspired polydopamine (PDA) has been investigated as a versatile coating on biodegradable metals to improve biocompatibility and adhesion of functional coatings [33–36]. However, the fabrication of PDA requires a long period of immersion to form a coating with a deposition rate of 2 nm/h only which poses the corrosion risk of active metal [33]. Then, multi-step pre-passivation of the matrix with strong acid or base and oxidants additives with heavy metal elements such as Cu²⁺ have been applied [37–41]. However, the pretreatment prolongs the process and lowers the operability, while the oxidant additives could preferentially react with the more reductive Zn rather than promote the polymerization. The additive residue would compromise the therapeutic effect bringing about uncontrolled heavy metal ions release [42].

Herein, we propose a one-step deposition and additive-free strategy to fabricate a PDA coating on the surface of pure Zn. A layer of pit-free and uniform PDA coating with improved deposition rate was filmed on the pure Zn at the optimal reaction condition. Both PDA polymerization and surface corrosion of Zn were studied through the surface morphology and chemical states characterization. The corrosion behavior of PDA coated Zn was compared with bare Zn by electrochemical corrosion and *in vitro* degradation. The blood compatibility of modified Zn was characterized in hemolytic test, coagulation, and platelets activation. To broaden the functionality on the Zn surface, a double-coated structure was fabricated with a layer of PLGA filmed on PDA coated Zn, and the mechanical performance of which is verified via stress loading experiments.

2. Materials and methods

2.1. Matrix material preparation

Pure Zn (99.99%) produced in a rolling process was obtained from China New Metal Materials Technology Co., Ltd. The square samples (10 mm × 10 mm × 1 mm) were applied for immersion tests and surface characterizations. Standard dog-bone-shaped specimens were used in tensile tests. For all experiments and performance tests, the specimens were ground up to smooth surface mechanically, cleaned ultrasonically for 15 min each in acetone and ethanol. Ethanol was used in the whole polishing process instead of DI water to prevent the oxidation of Zn. Pretreated Zn was stored in ethanol and taken out 30 min before experiments, dried with Ar.

2.2. PDA deposition

Dopamine-HCl (Macklin Biochemical Co., Ltd., China) was dissolved in 10 mmol/L Tris buffer to 2 mg/mL. The dopamine will be oxidized into dopamine quinone, intramolecular cyclization, and intramolecular structure rearrangement to generate 5, 6-dihydroxyindole in the solution, which can generate PDA through physical activity and chemical reactions such as self-polymerization, hydrogen bonding, and self-assembly [43–45]. The pH conditions of the dopamine-Tris solution were adjusted by 1 mol/L NaOH and 1.2 mol/L HCl to the pH of 7, 8.5, and 10, respectively. The reaction container was shaded to avoid oxidation

induced by light and placed in a magnetic agitator with a water bath at 25°C. Rapid polymerization of PDA in solution does not mean that the sample surface can be quickly coated. During the polymerization process, the PDA that has not effectively contacted on the sample surface in time will polymerize into microspheres and can scarcely film but float on the solution surface after the diameter increases gradually. Therefore, the elevated contact probability between PDA in the upper solution and Zn substrates at the bottom of the container could accelerate the coating process. The dopamine-Tris solution is stirred to inhibit the over accumulation of PDA at the solution surface and promote the diffusion of oxygen in the solution with the rotation speed of 150 r/min to ensure adequate, uniform oxidant (oxygen in the air) supply. Static solution without stirring has also been set to compare deposition results. After 6, 12, 24, 36, and 48 h immersion, the samples with PDA film were washed with deionized water three times, followed by drying with Ar. The deposition process scheme is shown in Fig. 1(a).

2.3. Surface and cross-section characterization

The surface morphology and roughness of coated samples were observed by atom force microscopy (AFM) with a frequency of 0.99 Hz. Scanning electronic microscopy (SEM) and energy dispersive spectroscopy (EDS) were employed for surface and cross-section investigation of coated samples. The surface chemical status of coated and double-coated specimens was characterized by Fourier transform infrared spectroscopy (FT-IR), Raman spectroscopy, and X-ray photoelectron spectroscopy (XPS).

2.4. Electrochemical corrosion tests

The coated structures and bare Zn samples obtained under different preparation parameters were applied to electrochemical tests on the CHI660E electrochemical workstation (Shanghai Chenhua Instrument Co., Ltd., China). A conventional three-electrode arrangement was employed. The sample (exposed area 0.28 cm²) was used as the working electrode, a platinum mesh (20 mm × 20 mm) was used as the auxiliary electrode, and a saturated calomel electrode (SCE) was used as the reference electrode. The electrolyte was simulated body fluid (SBF) solution, and the solution volume was 400 mL at 37 ± 0.5°C. Before the tests, all the samples were stabilized in SBF for 30 min. The electrochemical impedance spectroscopy (EIS) was tested with the frequency range of 10⁵–10⁻² Hz, and the disturbance amplitude was 10 mV. The potentiodynamic polarization (Tafel) curve was tested with a scanning speed of 1 mV/s.

2.5. Immersion degradation studies

Referring to Uniform Corrosion Methods of Laboratory Immersion Testing (JB/T 7901-1999), the samples were immersed with SBF (pH=7.2) (Shanghai Yuanye Bio-Technology Co., Ltd., China) to investigate coating structure *in vitro* degradation. The exposed area ratio of the samples in the solution was 1/20 cm²/mL, and the samples were placed in a constant temperature incubator at 37 ± 0.5°C. After soaking for 1, 7, 14, and 28 days, the samples were removed from the solution and washed three times with deionized water, gently dried with Ar. The samples were used for surface/interface observation and weight loss tests.

2.6. In vitro blood compatibility

Hemolysis, blood coagulation, and platelets adhesion of blood-contacting matrixes are essential reactions after being implanted.

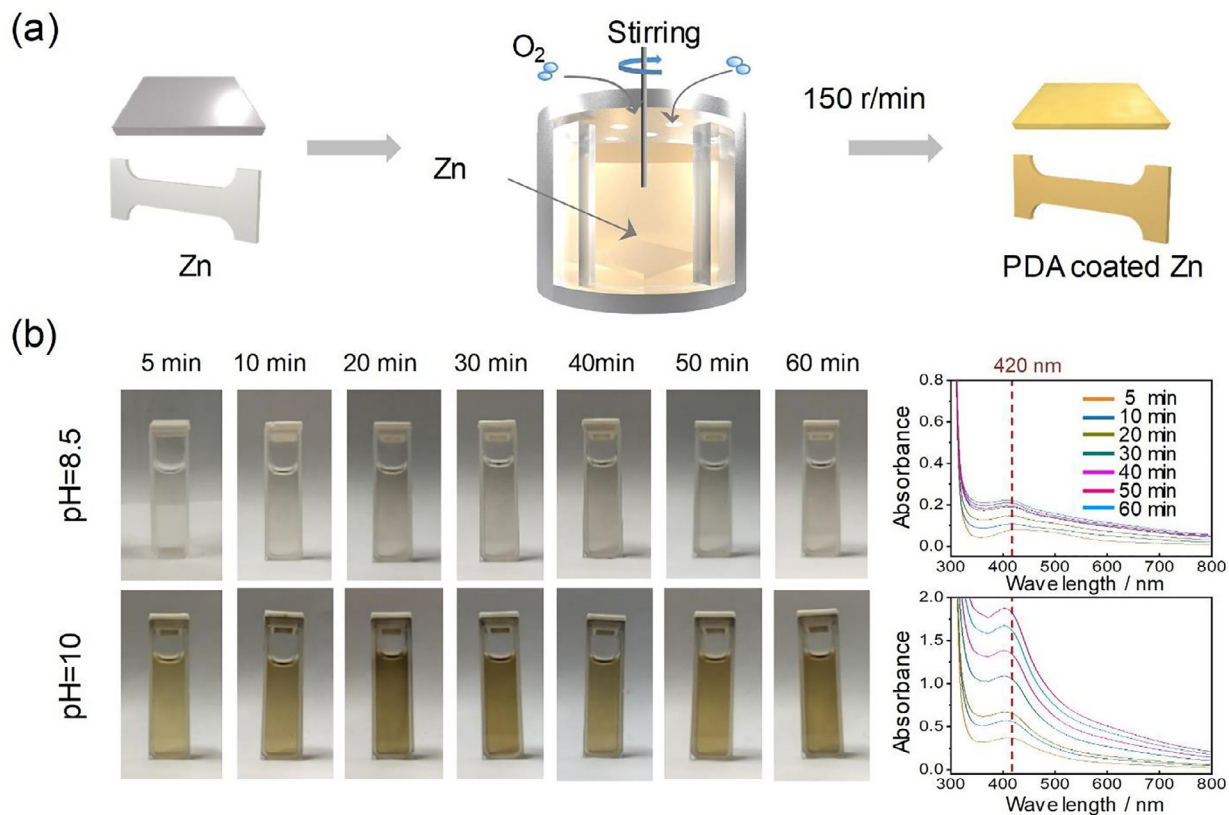


Fig. 1. (a) Processing diagram of PDA coating on pure Zn surface process with solution stirred, (b) photographs of dopamine polymerization and solution absorbance at 420 nm in different pH dopamine-Tris solutions at various time.

Blood for the *in vitro* blood compatibility experiments was obtained from healthy volunteers using anticoagulated blood collection tubes containing sodium citrate (1:9). Based on the requirements of ISO 10993–2017, all the tested samples were immersed in tubes with 10 mL physiological saline for 30 min at 37 ± 0.5°C. Physiological saline and sterile water with the same volume were set as the negative and positive control for the hemolysis test, respectively. Then the tubes were co-incubated with 0.2 mL whole blood diluted with physiological saline (4:5) at 37 ± 0.5°C. After 60 min reaction, all solutions were transferred into new tubes and centrifuged at 1000 rpm for 5 min. The absorbance of supernatant from each tube was measured by a microplate reader (Thermo Scientific, USA) at 545 nm. The hemolysis was calculated according to Eq. (1):

$$\text{Hemolysis}(\%) = \frac{\text{OD}(\text{test}) - \text{OD}(\text{negative})}{\text{OD}(\text{positive}) - \text{OD}(\text{negative})} \times 100\% \quad (1)$$

The coagulation tests were conducted through prothrombin time (PT), activated partial thromboplastin time (APTT), thrombin time (TT), and fibrinogen (FIB) assays. Platelet-poor plasma (PPP) obtained by centrifuging at 3000 rpm was incubated with different coated Zn samples with a ratio of 6 cm²/mL for 15 min. The tube that contained PPP without sample incubation was set as negative control (NC) group. After incubation, the PT, APTT, TT, and FIB values of all wells were determined through the CS-5100 coagulation analyzer (SYSMEX, Japan).

The fresh platelet-rich plasma (PRP) centrifuged at 1500 rpm from whole blood was incubated with various coated Zn specimens of 0.5 mL per well. After incubation for 30 min, the specimens were washed and prepared for platelets fixed with glutaraldehyde solution followed by gradient dehydration and de-alcoholization [46]. Then, the specimens were observed by SEM

to explore the platelets' morphological features and adhesion. All the blood biocompatibility tests were carried out in three replicates.

2.7. PLGA coating fabrication

PLGA is one of the most versatile biomedical polymers that can be tailored to acquire desirable features and drugs for controlling bioactive payload or stents matrix [47–49]. To explore the property of fabricating multifunctional treating instruments with PDA coated Zn, the polymer material PLGA was used to film on PDA coated Zn structure. Solid PLGA (Macklin Biochemical Co., Ltd, China) was dissolved with acetone by stirring the samples at 250 r/min without acetone volatilization to obtain a PLGA-acetone solution of 11.26 wt.%. The uniform PLGA film was prepared on the dry pure Zn, or PDA coated Zn surface by the drop casting method. The droplet coating amount of PLGA-acetone solution was 15 μL/cm². After PLGA was coated on the surface, the samples were put into an incubator of 37 ± 0.5°C for drying.

2.8. Mechanics tests

Nanoscratch and tensile tests were employed to estimate the adhesion force between coatings and substrates. Loading by the Nano Indenter G200 (Agilent, USA), the total scratch distance of the diamond indenter was 300 μm with a uniformly charging loading force from 0 mN to 200 mN, with the moving rate of 30 μm/s. Test areas were randomly selected on the surface of the sample at a certain distance from each other. Tensile tests were used to simulate the expansion deformation of stents. All the coated and uncoated specimens were stretched by AGXplus (Shimadzu, Japan)

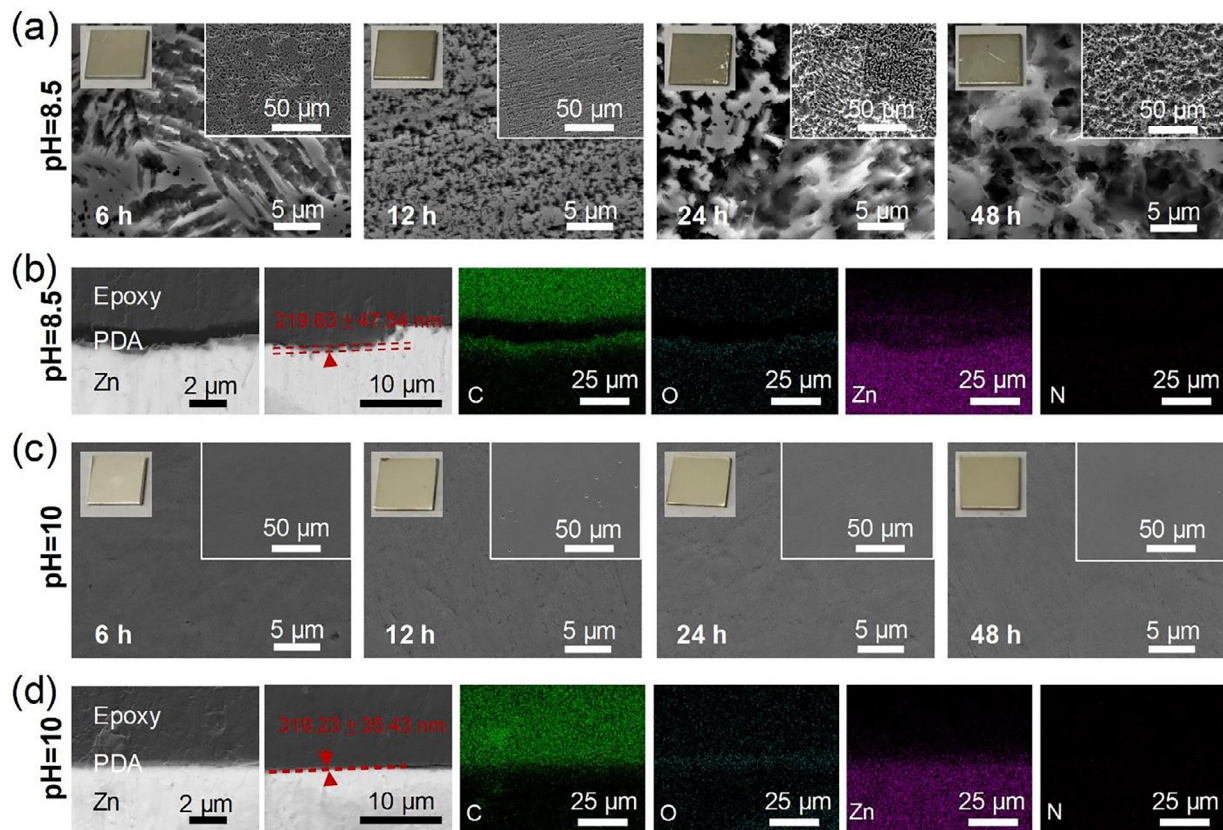


Fig. 2. (a) Surface morphology SEM image of PDA coated Zn under pH=8.5 condition at various time, (b) cross-section SEM image and EDS mapping of PDA coated Zn under pH=8.5 condition, (c) surface morphology SEM image of PDA coated Zn under pH=10 condition at various time, (d) cross-section SEM image and EDS mapping of PDA coated Zn under pH=10.

with a 1 mm/min stretching rate. At the end of the experiment, the fracture morphology and deformation state of the coating on the sample surface were analyzed.

3. Results and discussion

3.1. PDA synthesis and surface coating

The effects of pH change on PDA polymerization were studied by observing the UV-Vis absorbance of the reaction solution. With the alkalinity of the solution gradually increasing, the color of the PDA-Tris reaction solution changed from only slightly gray to deepen evidently (Fig. S1(a) in Supplementary Information and Fig. 1(b)). The characteristic absorption peak of PDA is at 420 nm [50], and the absorbance gradually moved up in Figs. S1(b) and 1(b). The increasing concentration of OH⁻ in the solution promoted the reaction to the right in the dopamine-to-quinone oxidation reaction step consistent with Fig. S1. The absorbance of the pH=10 sample increased most obviously with the increase of reaction time.

The coating process with different pH values and solution statuses was compared in Fig. S2(a) (static) and S2(b) (stirred), respectively. All static deposited Zn owned the surface with corrosion pits, and the pH=8.5 sample was the most corroded. When the pH=7 solution was stirred, the stepped corrosion morphology of the sample surface was highly obvious with corrosion steps (Fig. S2(b)). The corrosion phenomenon on the surface of the pH=8.5 sample was more evident (Figs. S2(b), 2(a)) than that of the static immersion coated sample with nano-sized particles aggregation. It indicates that PDA coating has been successfully deposited on the surface of the Zn substrate, but the deposition effect is not uni-

form. The stirred pH=10 sample surface showed pit-free and uniform morphology (Figs. S2(b) and 2(c)), proving that the surface was hardly porous corroded.

In the interface of SEM observation (Fig. 2(b)), the stirred pH=8.5 sample showed micron grade of ups and downs had uneven gray coating samples in line with surface morphology. In the EDS mapping, the inter-layered structure was a rich source of C, O, and Zn elements, which should be the deposition of PDA coating and the mixture of Zn surface corrosion products. There was an obvious coating layer observed in pH=10 samples. EDS mapping (Fig. 2(d)) illustrated that the coating was rich in C and O elements and contained a small amount of N element, proving the PDA coating generated. With cross-sections randomly selected and the thickness statistics made, it was found that the thickness of the corrosion product plus PDA layer in pH=8.5 sample was about 219.6 ± 47.5 nm, while the thickness of the PDA coating in pH=10 sample was 319.2 ± 35.4 nm. The pH-modified deposition processes significantly increase PDA coating thickness by over 45% with more smooth surface morphology and over 6 times than reported deposition rate.

3.2. Surface morphology and chemical composition

In the AFM observation, the surface of Zn in stirred solution with pH=7 exhibits stepped corrosion morphology which is the typical corrosion morphology of Zn in dopamine-Tris solution at low pH (Fig. S3(a)). Hill-like corrosion morphology appeared on the pH=8.5 sample surface after stirring, as shown in Fig. S3(b), which is the optimal micro-alkaline condition for depositing PDA coating on common substrates [33]. It proved that the film formation of PDA was competing with the Zn surface corrosion. No

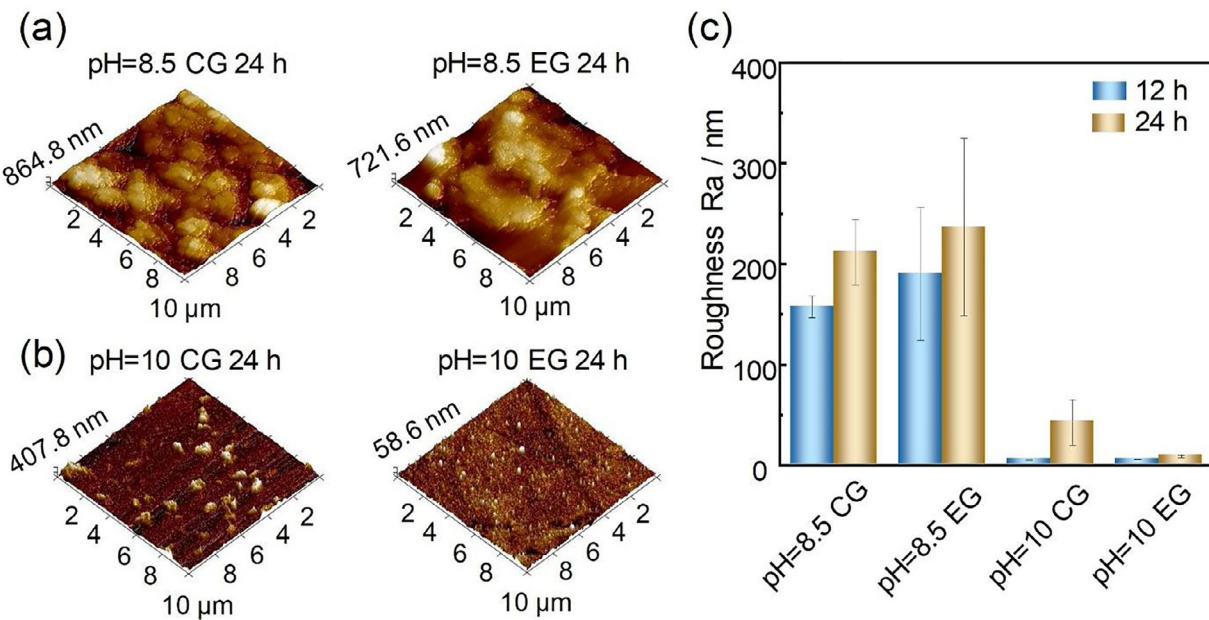


Fig. 3. (a) Three-dimension surface topography image of pH 8.5 CG and pH 8.5 EG, (b) three-dimension surface topography image of pH 10 CG and pH 10 EG, (c) roughness comparison of different surface processing.

corrosion occurred on the pH=10 sample (Fig. S3(b)). The fluctuation of the sample surface gradually increased with the extension of deposition time caused by the increase of the coating thickness. A control group (CG) was used to distinguish from the experiment group (EG) to explore the effect of the Tris solution on the surface. The CG sample was immersed in a Tris buffer of different pH without adding dopamine for different periods (12 and 24 h) (Fig. 3(a) and (b)). The slight scratch and minor morphology fluctuations of the EG sample proved the formation of the PDA coating on the surface. However, on the pH=10 CG 24 h sample, hundreds of nanometers-high corroded particles were detected, which should be the corrosion products produced by Cl⁻ from Tris [51,52]. The value of surface roughness is in keeping with morphology images. Higher pH samples owned lower roughness Ra value with less non-uniform corrosion in both CG and EG groups, as shown in Fig. 3(c). The Ra values of pH=8.5 CG and EG samples were all over 150 nm and the results are significantly fluctuated after both 12 and 24 h processing. The pH=10 samples have lower values such as 6.0 ± 0.7 nm, 43.0 ± 22.6 nm at CG condition after 12 and 24 h, and 6.0 ± 0.3 nm, 9.1 ± 1.3 nm at EG condition after 12 and 24 h, respectively. These results match the surface morphology according to the corrosion behavior in different pH conditions. Additionally, 24 h deposition process brings higher consistency and lower surface roughness in the pH=10 deposition process. Based on the PDA film formation and surface corrosion, it is practical to fabricate PDA coated Zn in the stirred process up to 24 h at the pH=10.

Chemical status study on the various surface was explored through the XPS spectrum in Fig. 4(a–c). The C 1s spectrum on the surface of bare Zn can be divided into C-C/C-H, C-N/C-O, C=O, and O-C=O groups by peak splitting, which are carbon pollution peaks caused during sample preparation and storage in the atmospheric environment [53,54]. The C-N/C-O peak of PDA-coated samples, which moved 0.5 eV towards the direction of low binding energy, was located at 286 eV. The shift of the peak indicates that the content of the C-N bond increases in PDA coating consistent with the presence of amino in the PDA structure. The C=C peak was observed at 284 eV in the coated samples corresponding to the unsaturated C=C bond in the aromatic ring

of dopamine [55]. In the O 1s peak, the surface of bare Zn is mainly composed of surface Zn-O, C=O, and C-OH groups [44]. N 1s peaks of PDA coated samples were divided into aromatic nitrogen bonds, C-NH and C-NH³⁺ [44]. The signal intensity of Zn 2p on the surface of the pH=10 sample decreased without the chemical composition of the sample surface changing, proving that the rapid deposition of PDA is beneficial to isolate the reaction of the Zn surface. At the same time, it was mutually verified with no Zn-O peak detected in the O 1s peak, indicating that the deposited PDA coating was highly dense. On the contrary, a peak (BE = 1025.4 eV) was detected on the surface of the pH=8.5 sample on behalf of the corrosion products produced by Tris buffer, water, and carbon dioxide in air during the coating process.

Further study through Raman spectrum found that the 570 cm⁻¹ and 800 cm⁻¹ peaks of bare Zn samples correspond to the presence of Zn-O and surface organic pollutants, respectively (Fig. 4(d) and (e)). The peak on the surface of pH=8.5 EG at 1573 cm⁻¹ and 1329 cm⁻¹ corresponds to the deformation vibration and stretching vibration of catechins (Fig. 4(d)) [56]. The surface peaks of pH=10 samples were similar to those of pH=8.5 samples, and there were deformation and stretching vibration peaks of catechins and benzene rings (Fig. 4(e)) [57,58]. Moreover, at pH=10, the oxidative polymerization of dopamine on the sample surface also resulted in a blue shift of benzene stretching vibration peak. In the FT-IR spectrum (Fig. 4(f) and (g)), the vibration peak of Zn oxides near 500 cm⁻¹, a C-OH vibration peak at 600 cm⁻¹ appeared on bare Zn [59,60]. C-H and O-H/N-H stretch vibration peaks exist at 2850–2950 cm⁻¹ and 3100–3600 cm⁻¹ [58]. It indicates that the surface of bare Zn is mainly composed of the natural oxide layer, Zn(OH)₂, and organic pollutants. Different from the Raman spectrum, the FT-IR peaks of the control groups exhibited more absorption peaks. These peaks belong to the corrosion deposition products generated by Tris on the sample surface, but the vibration corresponding to these peaks lacked Raman activity. The C-N stretching vibration in Tris primary amine was located at about 1160–1100 cm⁻¹, and weak absorption signals were detected only in the pH=8.5 control group.

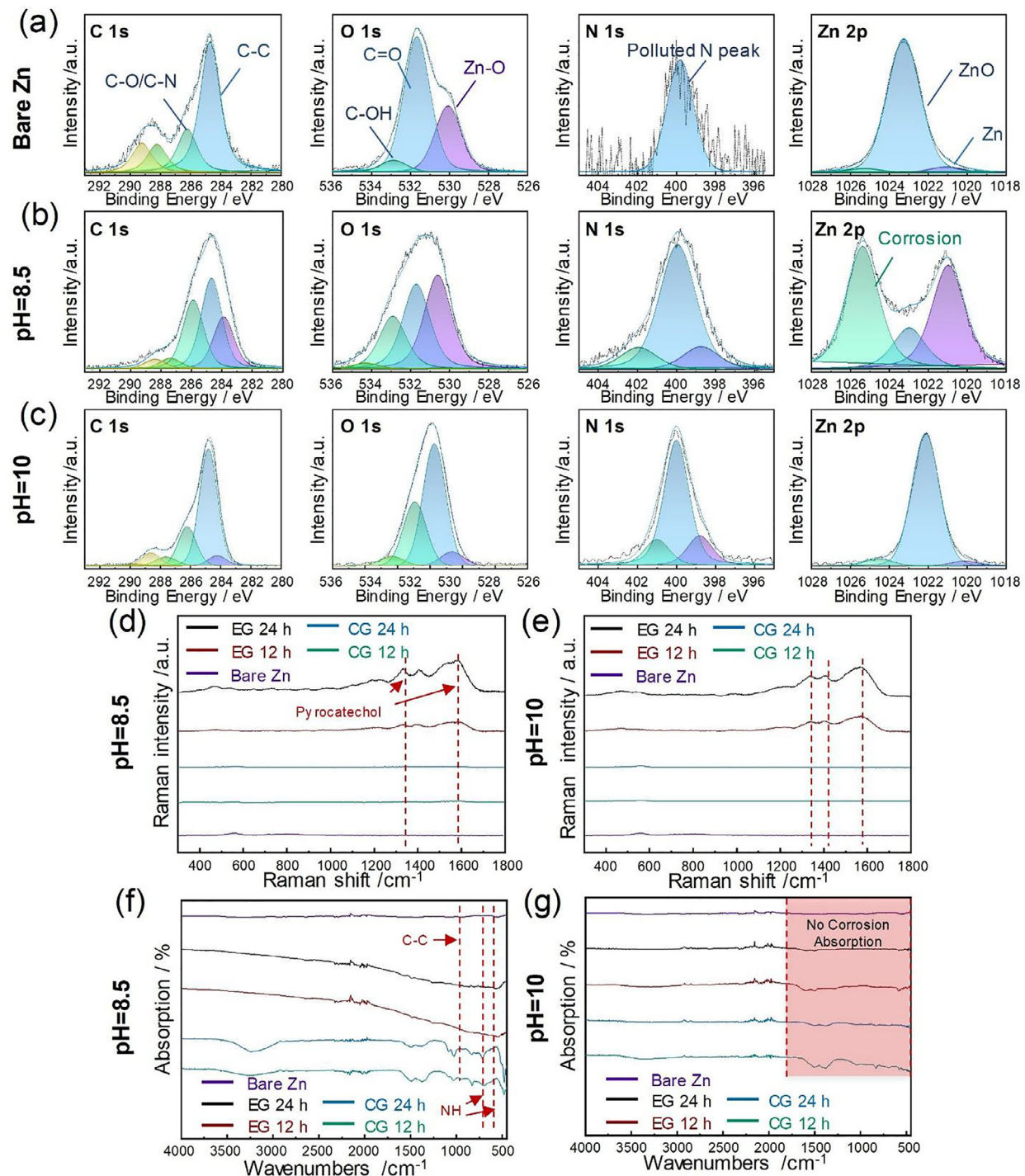


Fig. 4. C 1s, O 1s, N 1s and Zn 2p XPS spectra of (a) pure Zn surface, (b) pH=8.5 surface and (c) pH=10 surface; (d) FT-IR spectra and (e) Raman spectra of pH=8.5; (f) FT-IR spectra and (g) Raman spectra of pH=10.

3.3. Coating construction mechanism

According to the observation and analysis of physical and chemical characteristics on the surface, under the condition of a lower OH⁻ concentration, oxidative polymerization deposition of dopamine does not normally occur. Meanwhile, severe corrosion of the Zn surface occurs, with the autocatalysis effect of Cl⁻ in Tris solution, pitting corrosion displays (reaction [1] and [2]) [51,52]. Due to the slow deposition rate of PDA, the coating formed will be peeled off in the Zn corrosion process rather than filmed, lead-

ing to hardly observing deposited the PDA coating on the surface. When the solution presents weak alkalinity, the surface of bare Zn converts into ZnO and stably exists (reaction [3]). However, the corrosion product ZnO generates on the sample surface unequally and slowly during the pH=8.5 immersion process, resulting in a loose corrosion product layer that can scarcely shield the continuous Cl⁻ corrosion. With insufficient generated PDA available in the solution, it is difficult to develop a thick enough film (Fig. 5(a)). Under the condition of pH=10, the concentration of OH⁻ in the solution is high, and the sample surface can be rapidly oxidized and in a

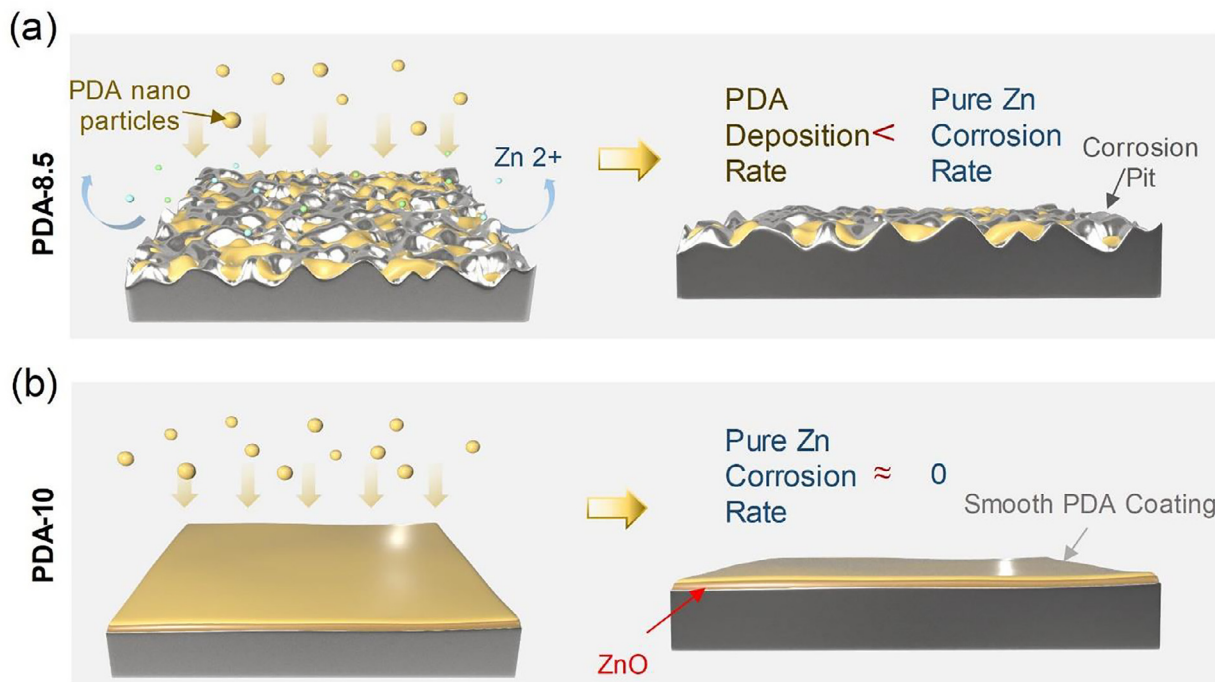


Fig. 5. Schematic drawing of (a) fabrication at pH=8.5 with corrosion pits produced and (b) uniform pit-free surface fabricated at pH=10 condition.

stable form of ZnO in the solution. At the same time, dopamine can rapidly polymerize under this condition so that PDA coating can be effectively formed on the surface with a rapidly passivated and dense ZnO layer (Fig. 5(b)). The samples fabricated by the optimal coating process were named PDA-10 distinguished with samples at pH=8.5 designated PDA-8.5. Bare samples were set as the blank group (pure Zn) to compare with the PDA coated Zn.



3.4. In vitro degradation behavior

The degradation study was carried out in SBF solution at $37 \pm 0.5^\circ\text{C}$, as shown in Fig. 6(a). During the degradation process, the surface of pure Zn gradually deepened from silver-white. With the continuous degradation, the corrosion product was thickness up to several micron thicknesses. Some deep pits could be observed in local areas from the cross-section observation, which is similar to other reports [61,62]. White corrosion products were observed in the light-colored area on the surface of PDA-8.5. After 28 days, the rough surfaces of PDA-8.5 were almost joined together, while the stepped corroded structures inside remained. The corrosion layer is connected into a sheet with a thickness of about $2 \mu\text{m}$. The PDA-10 surface darkened during degradation and gradually changed to yellow after 28 days, and the density of corrosion products on the surface of PDA-10 was the lowest in the form of nanoparticles. A thick corrosion layer appeared on the PDA-10. With the increase of time, a continuous corrosion layer with a thickness of about 700 nm was obtained on the surface of PDA-10. The Zn matrix was closely connected to the corrosion layer, and the morphology was very smooth and uniform.

After the degradation process, the mass loss of pure Zn was 0.40 mg , while the mean mass loss of PDA-8.5 and PDA-10 were

Table 1
Fitting results of the polarization curves.

Specimens	Pure Zn	PDA-8.5	PDA-10
$E_{\text{corr}} (\text{V})$	-1.17	-1.15	-1.14
$i_{\text{corr}} (\mu\text{A cm}^{-2})$	38.88	90.56	52.28

0.30 mg and 0.25 mg , respectively (Fig. 6(b)). Uncoated pure Zn suffered the maximum mass loss with the continuous matrix corrosion after being degraded *in vitro* for 28 days. Although it was observed from SEM results that the PDA coating on the surface of the other samples dissolved and fell off, the mass loss was still lower than that of Zn. The PDA-10 samples with a continuous corrosion layer loss minimum matrix mass. Compared with uncoated pure Zn, the corrosion rate of PDA-8.5 and PDA-10 decreased by 11.0% and 28.8% derived from the corrosion rate in Fig. 6(c), respectively. The coating of PDA can induce the formation of relatively dense corrosion products on the surface of pure Zn, which can reduce pitting corrosion and dissolution of metal ions in the early implantation stage to a certain extent.

3.5. Electrochemical performance

With the increase of voltage, the passivation-like area appeared in the anode of the three samples, which proved that the corrosion production would accumulate on the sample surface, which could prevent the surface corrosion from the polarization curves (Fig. 7(a)). The corrosion potential and corrosion current density of the samples were obtained, as shown in Table 1. The higher the corrosion potential of the sample, the more difficult it is to be corroded. The corrosion potential and corrosion current density of the samples increased after PDA coating. It indicated that the PDA coating could also prevent corrosion in the early stage. The results calculated from the polarization curves using Tafel fitting are summarized in Table 1. However, the corrosion rate of the sample would increase after the coating falls off or further corrosion

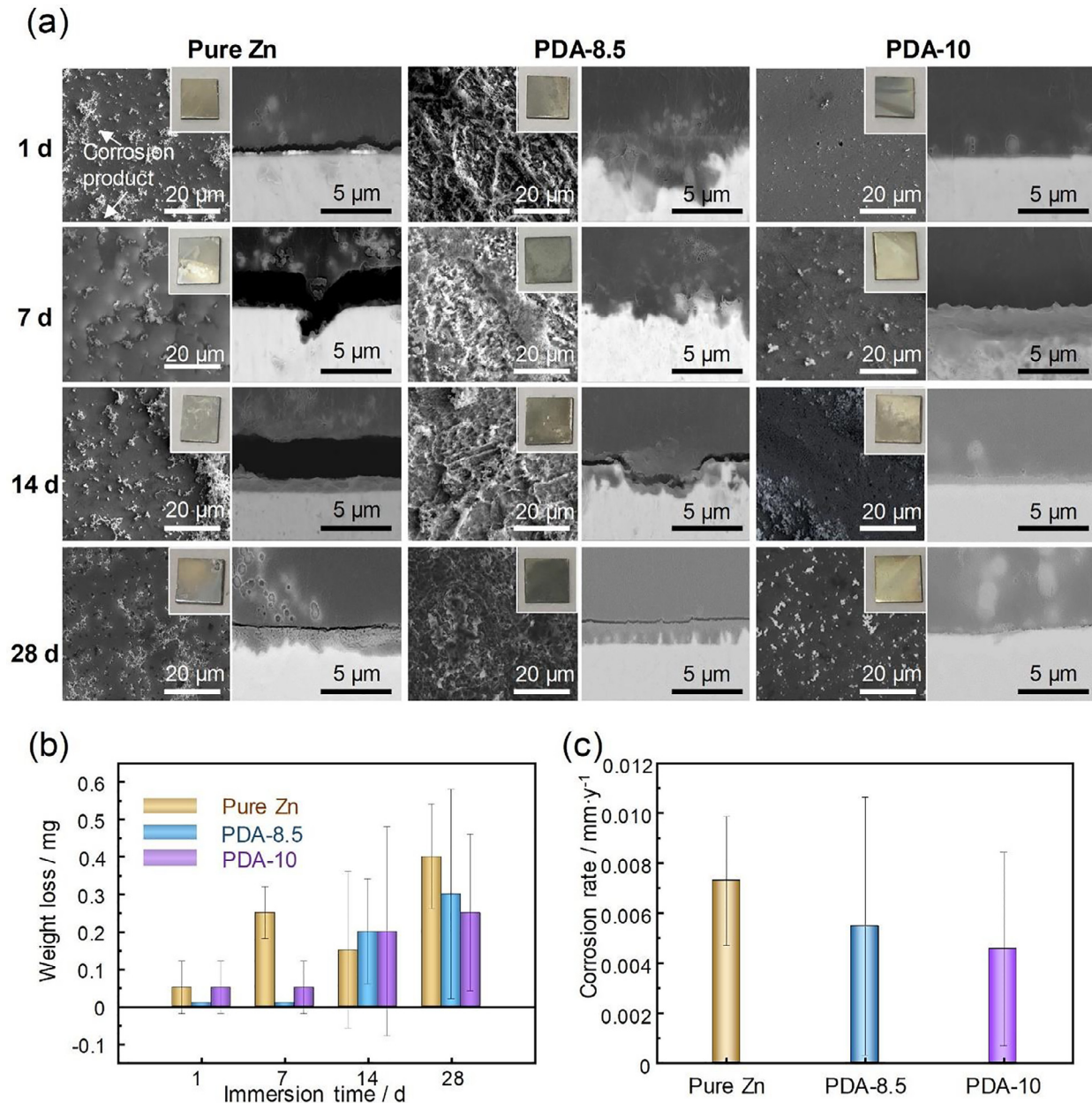


Fig. 6. (a) Surface morphology and cross-section image of pure Zn, PDA-8.5, and PDA-10 during 28-day immersion degradation studies, (b) weight loss of different groups as a function of immersion time, (c) corrosion rate of different groups.

occurs, which is similar to the phenomenon observed in previous studies on PDA coated Mg [34–37].

In Nyquist plots depicted in Fig. 7(b), it was found that the capacitive loop of pure Zn was observed in both high-frequency and low-frequency regions with the smallest arc radius, which is the sample group most prone to corrosion. The capacitive loop of PDA-8.5 was not the largest, which proves that the bonding formed between PDA and Zn was hardly tight, or the deposition of PDA coating is not dense due to the deposition process generated corrosion. The large arc radius of the PDA-10 sample proves that it has strong corrosion resistance. The PDA-10 sample of low-frequency impedance modulus $|Z|$ was more significant (Fig. 7(c)); that is, the sample surface structure is more excellent corrosion resistant performance. In the phase-frequency diagram (Fig. 7(d)), the low-frequency phase angle of the pure Zn sample is close to

45° on behalf of the diffusion behavior on the surface of pure Zn.

The PDA coating can increase the corrosion resistance of pure Zn based on the plots discussed above. Equivalent circuit (EC) models, as shown in Fig. 7(e), were adopted to fit the EIS spectrum to explain EIS spectrum results more accurately. The EC1 circuit $R_s(Q_1(R_1(Q_2(R_2W))))$ is used to fit the EIS curve of pure Zn in SBF solution. R_s represents the solution resistance, Q_1 and R_1 represent the double layer capacity and charge transfer resistance, and Q_2 and R_2 represent the capacitance and resistance of corrosion products in the high-frequency region. W is the diffusion impedance in the low-frequency region. Q , as a constant phase element, is used to replace ideal capacitance C to compensate for the non-uniformity (such as porosity, roughness, etc.) and the presence of adsorption on the surface of the test sample. The EC2 circuit

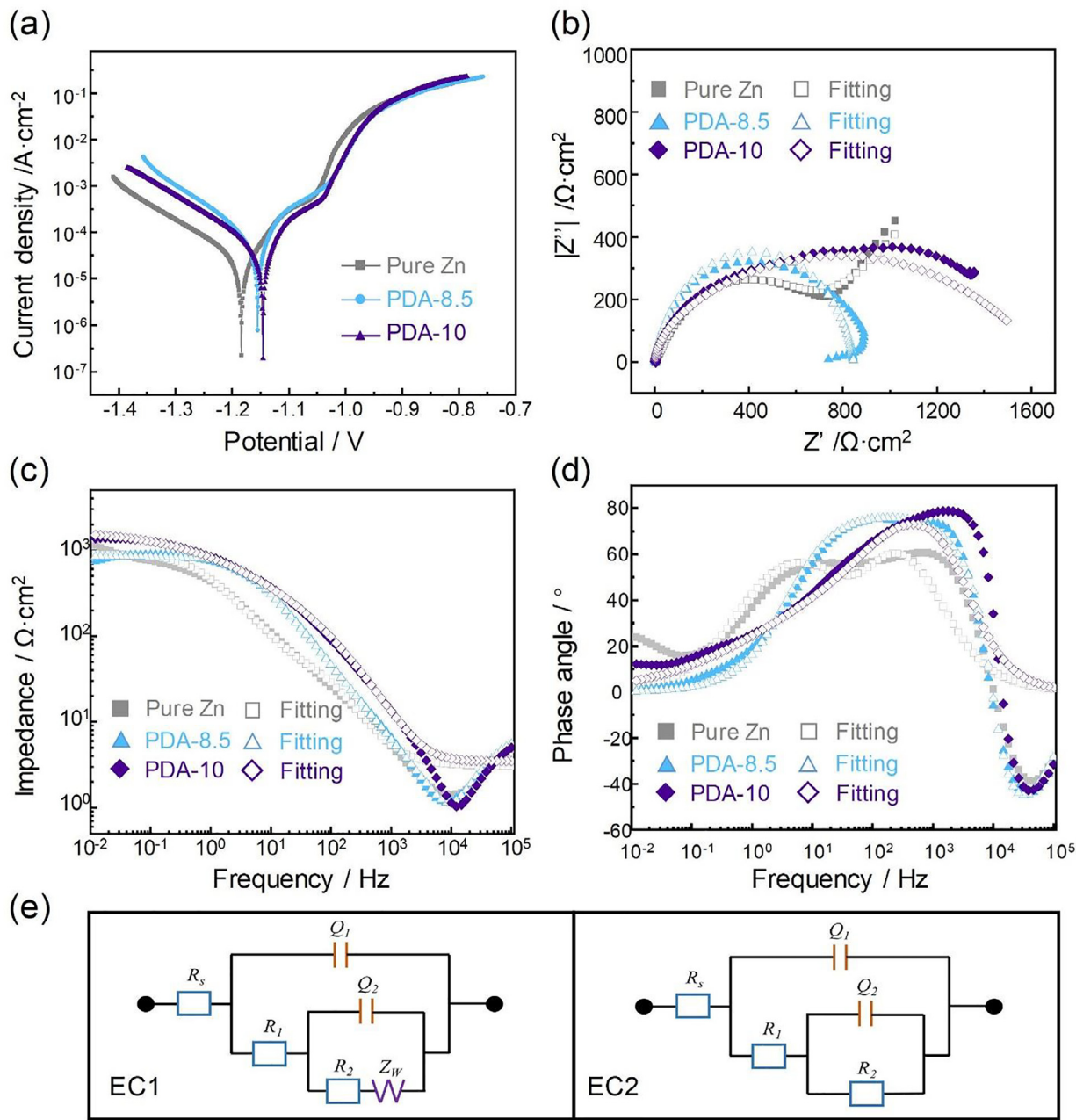


Fig. 7. (a) Potentiodynamic polarization curves of pure Zn, PDA-8.5 and PDA-10 in SBF solution, (b) Nyquist plots and fitting curves of different groups in SBF solution, (c) Bode plots of impedance vs. frequency, (d) phase–frequency diagram, (e) equivalent circuits models of bare and coated samples.

$R_s(Q_1(R_1(Q_2R_2)))$ is used to fit the EIS curve of the PDA coated Zn structure. The corrosion product layer resistance R_1 and charge transfer resistance R_2 of the PDA coating surface were increased after the PDA coating was deposited. The results consistent with the polarization curve illustrated that the PDA coating could slow down the corrosion of pure Zn at the initial stage of immersion. The higher charge transfer resistance of PDA-10 samples indicated a layer of zinc oxide which is relatively more resistant to corrosion between Zn and PDA coating consistent with the deposition concluded before. The results of fitting two equivalent circuits for EIS are shown in Table 2.

The polarization resistance R_p of the two equivalent circuits is calculated using the difference between the actual impedance and R_s on the Nyquist diagram when the frequency drops to zero. R_1 , R_2 , and R_L of the above samples in SBF solution were summarized to obtain the polarization resistance R_p . The R_p calculation formula

Table 2
Fitting results of EIS.

Specimens	Pure Zn	PDA-8.5	PDA-10
R_s ($\Omega \text{ cm}^2$)	3.03	3.59	3.49
CPE_1 ($10^{-5} \text{ S cm}^{-2} \text{ s}^n$)	3.85	2.78	1.24
n_1	1.00	1.00	1.00
R_1 ($\Omega \text{ cm}^2$)	31.44	107.34	92.70
CPE_2 ($10^{-5} \text{ S cm}^{-2} \text{ s}^n$)	32.85	9.74	32.94
n_2	0.76	0.70	0.47
R_2 ($\Omega \text{ cm}^2$)	653.04	767.81	1569.55
W ($10^{-3} \text{ S cm}^{-2} \text{ s}^{0.5}$)	1.90	-	-

las of the two equivalent circuits are as follows as Eqs. (4) and (5), and the results are calculated in Table 3. After being coated with PDA, the R_p of the samples increased continuously. In particular,

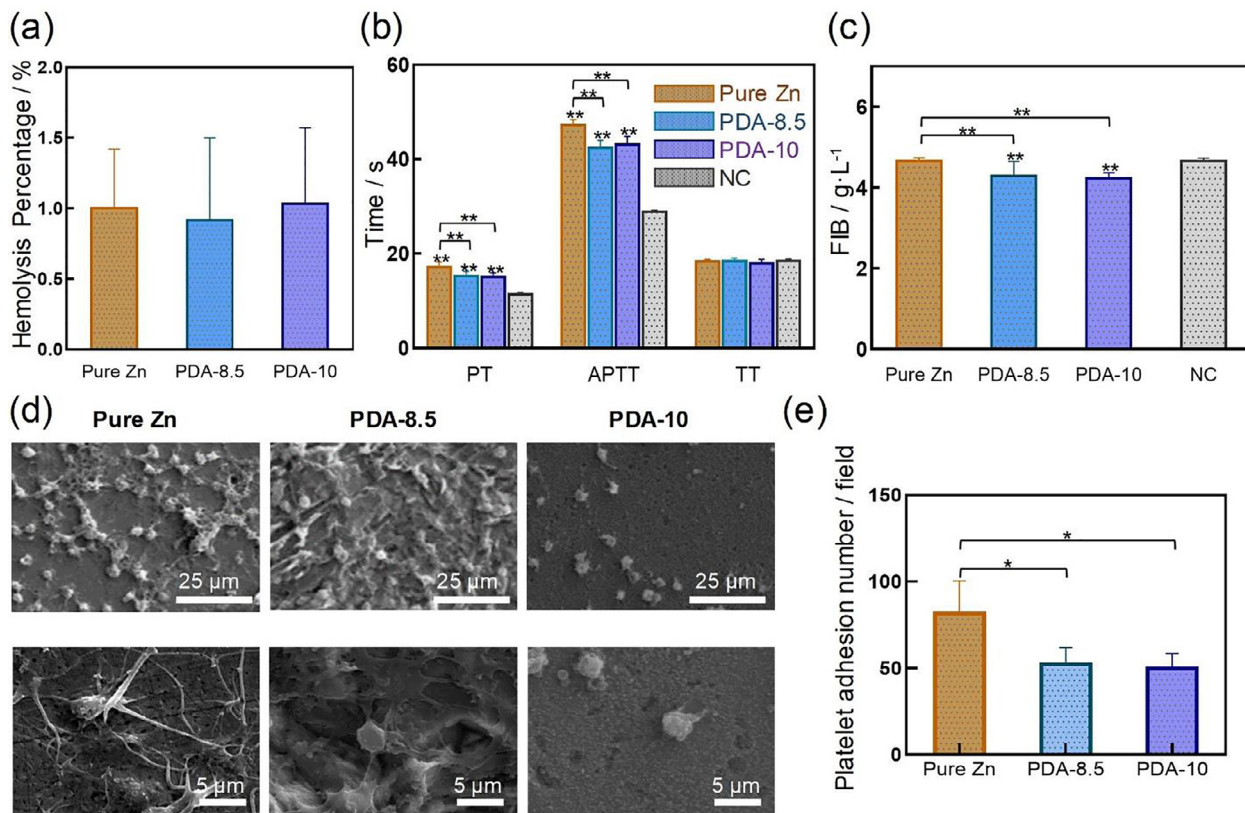


Fig. 8. (a) Hemolysis percentage, (b) APTT, PT, and TT, (c) FIB, (d) performance of adhered platelets, (e) platelets assembled number (per 2000× field) ($n=3$) of bare and coated samples. Statistically significant difference is indicated by * $p < 0.05$, ** $p < 0.005$, using a one-way ANOVA.

Table 3
Calculation of polarization resistance R_p .

Specimens	R_p (Ω)
Pure Zn	686.38
PDA-8.5	875.15
PDA-10	1662.25

PDA-10 has over twice the R_p of pure Zn.

$$\text{EC1} : R_p = R_1 + R_2 + W \quad (4)$$

$$\text{EC2} : R_p = R_1 + R_2 \quad (5)$$

3.6. In vitro evaluation of the hemocompatibility

Hemolysis, resulting from the rupture of erythrocytes, could lead to *in vivo* toxicity and oxygen transportation block. The three samples performed hemolysis as $1.01\% \pm 0.41\%$, $0.92\% \pm 0.58\%$, and $1.04\% \pm 0.53\%$, respectively, induced by direct contact with whole blood, as shown in Fig. 8(a). The hemolysis performance of PDA coated specimens shows no statistical difference compared to pure Zn. Moreover, all the hemolysis percentages are much less than 2% which indicates that both uncoated and coated samples are nonhemolytic materials [63]. The coagulation performances of different samples are shown in Fig. 8(b) and (c). The PT values of the three group samples are significantly longer than the NC group ($p < 0.005$), which exhibits the potential of anticoagulation. The APTT times of pure Zn, PDA-8.5, and PDA-10 are prolonged longer than the NC group significantly ($p < 0.005$), with an increase

of 5.8 s, 3.8 s, and 3.6 s, respectively. The PT and APTT results indicate that the PDA coated samples did not activate the extrinsic and intrinsic coagulation pathway. Though the difference between the two PDA coated samples is not significant, the results of PDA-10 samples were closer to the normal range of prothrombin and active partial thromboplastin function [64,65]. The TT results of tested groups are not significantly different from the NC group, which means that all the samples bring no impact on the common pathway of coagulation. The FIB values of both the tested group and NC group were slightly over the normal range (2–4 g/L) (Fig. 8(c)) [66]. The fibrinogen could adhere to the coated matrix due to the PDA coating with mentioned excellent adhesive properties.

Anti-platelet adhesion and platelet inaction are vital parts of good blood compatibility. PRP was co-incubated with pure Zn for 30 min, and a large number of platelets were found to completely spread and adhere to the surface of pure Zn (Fig. 8(d)). These adherent platelets were all activated with abundant pseudopodia stretched out. For PDA-8.5, platelet adhesion still exists on the surface with high roughness generated in the PDA coating process, and all of them show the activation state of pseudopodia spreading (Fig. 8(d)). However, due to the roughness of the surface, platelet adhesion produced in short-term incubation is less than that of pure Zn surface. If the incubation time with blood increases, it is possible to increase the number of platelets adhered to the surface. There were platelets on the surface of PDA-10, but almost all of them are normal and full spherical without pseudopodia (Fig. 8(d)). The platelet adhesion numbers of pure Zn, PDA-8.5, and PDA-10 samples were compared obviously that PDA coating can ease the platelet adhesion (Fig. 8(e)). The adhesion and activation of platelets are not simply dependent on the total amount of ad-

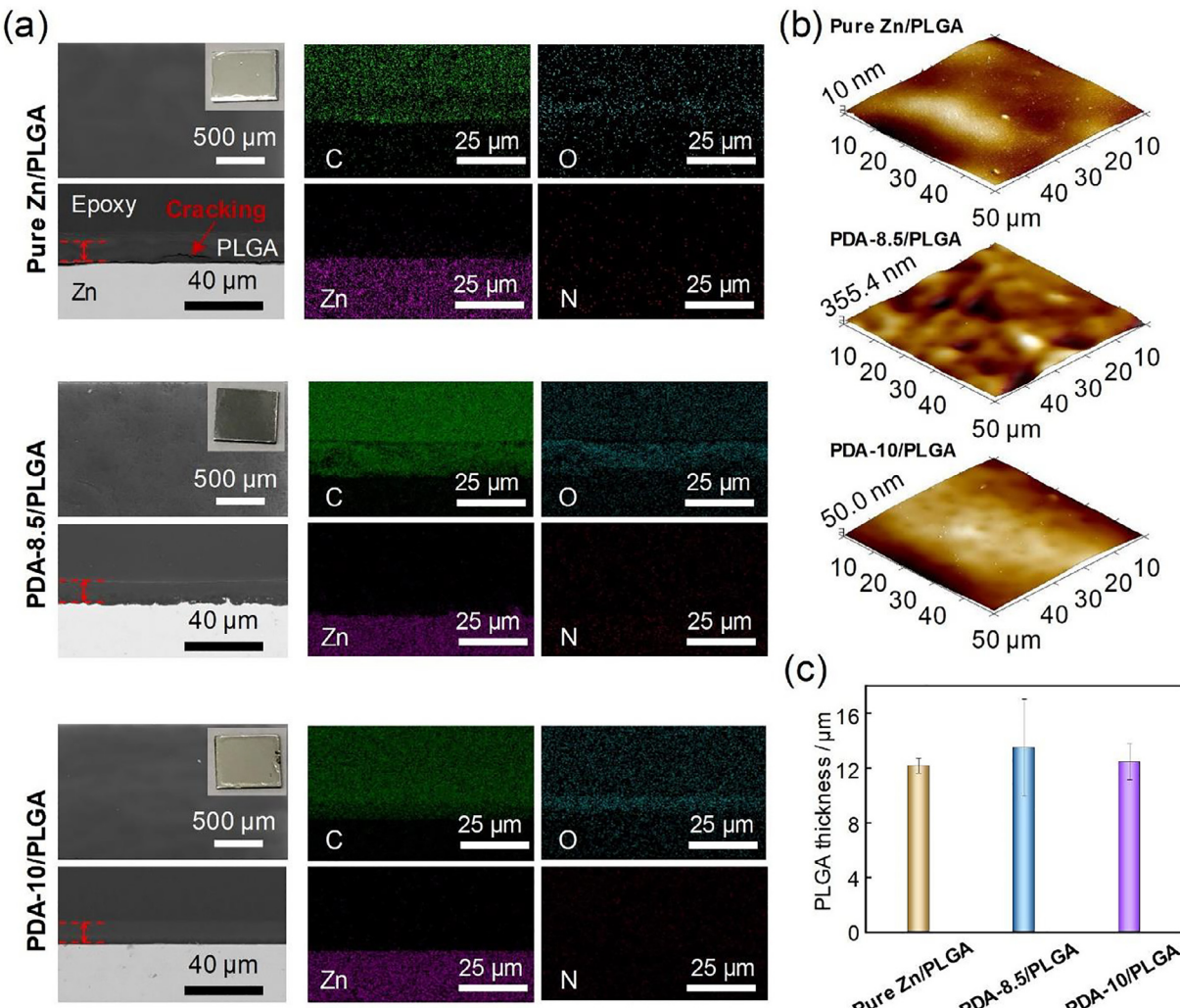


Fig. 9. (a) SEM image and EDS mapping, (b) three-dimension morphology with roughness labelled, (c) PLGA coating thickness of pure Zn/PLGA, PDA-8.5/PLGA and PDA-10/PLGA composite coated structures.

sorbed fibrinogen but rather on its conformation [67]. There it is shown that the performance of platelets adhesion and activation is not contradictory with the FIB results. These results indicate that PDA-10 samples perform the ability of anticoagulation and can inhibit platelet adhesion, aggregation, and activation to the coated devices proving the antithrombotic property of coated structures at the same time.

3.7. Double-coated structure characterization

PLGA filmed structure was fabricated and observed by optical images in Fig. 9. The PLGA coated samples of pure Zn and PDA-10 have smooth and pit-free surfaces, showing a complete and dense PLGA polymer surface, divided into pure Zn/PLGA and PDA-10/PLGA. However, on the surface of the PLGA coated PDA-8.5 sample, which was represented as PDA-8.5/PLGA, the presence of small bumps and scratches was observed. Due to the uneven corrosion morphology of the surface, the surface roughness was up to the sub-micron level. Therefore, on the PDA-8.5 surface with significant fluctuation, PLGA can reduce the surface roughness, but micron-level fluctuation and micro-pits can still be observed.

In further investigation (Fig. 9(a)), smooth PLGA coating was observed on pure Zn samples with partial coating fell off and slight

corrosion marks. At the PDA-8.5/PLGA interface, due to the PDA interlayer, the coating was closely connected to the substrate, and the element transition was smooth in the EDS mapping. The surface of the PDA-10/PLGA structure was smooth, and no obvious transition layer was found in the cross-section. PLGA can fill the holes and scratches left by pure Zn in the polishing process, lowering the height difference on the surface to 10 nm (Fig. 9(b)). The maximum height difference is 355.4 nm through the morphology image, indicating that PLGA can fill the corrosion morphology and pores induced by the coating process to flat the surface. However, it is still difficult to completely smooth the sub-micron fluctuations generated in the PDA coating process. The surface fluctuation of PDA-10/PLGA was slightly more significant than that of pure Zn/PLGA, and small particles existed on the surface. The results verified the existence of uniform PDA between PLGA and Zn substrate with the phenomenon of nanoscale polymerization clusters on the surface discussed before. The thickness of drop-casting fabricated PLGA film was analyzed in Fig. 9(c). The pure Zn/PLGA and the PDA-10/PLGA perform similar PLGA film thickness which are $12.2 \pm 0.6 \mu\text{m}$ and $12.5 \pm 1.3 \mu\text{m}$, respectively. The PDA-8.5/PLGA owns the slightly thicker PLGA coating with the thickness of $13.5 \pm 3.6 \mu\text{m}$ which is variable resulting from excessive surface corrosion of the PDA fabrication process.

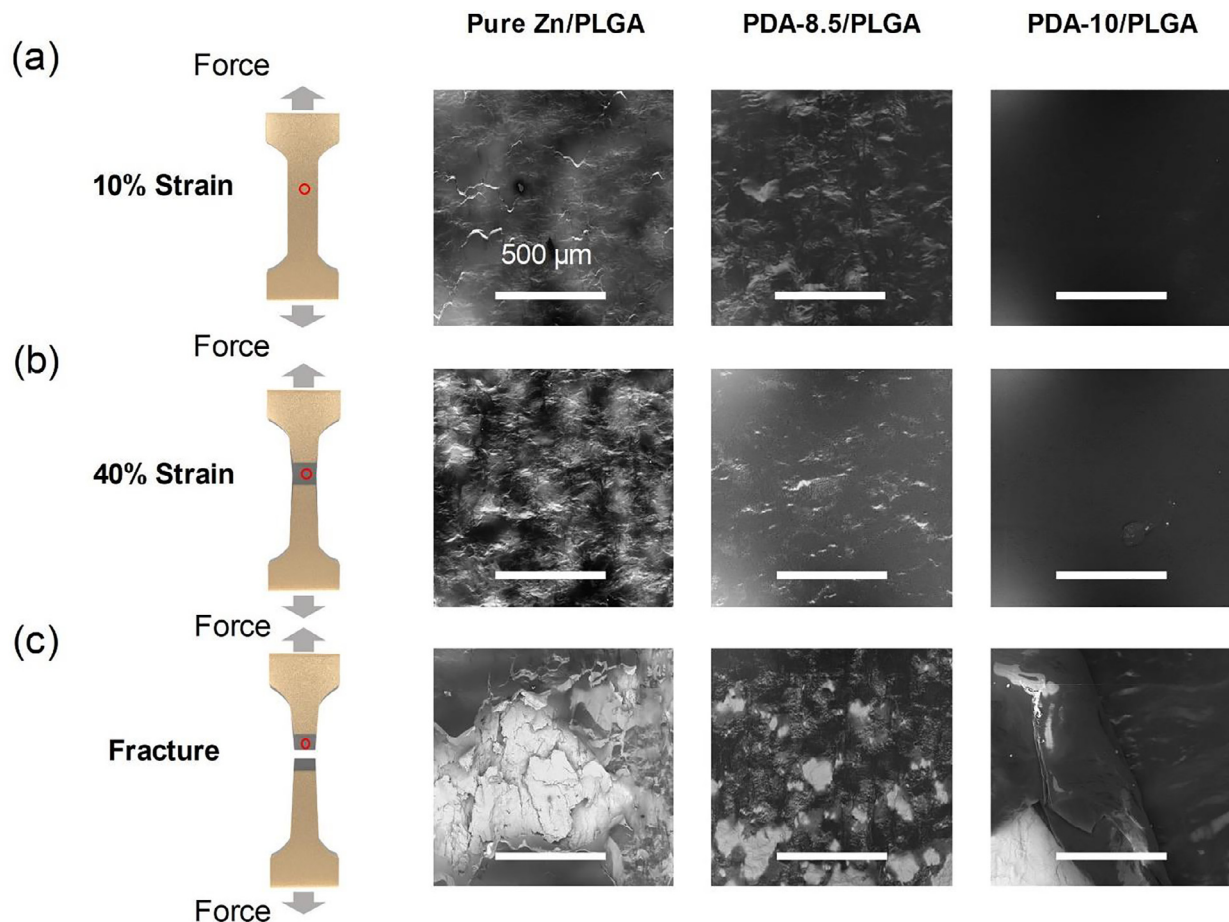


Fig. 10. (a) 10% strain, (b) 40% strain, (c) fracture tensile schematics and surface morphology from pulled composite coated structures.

3.8. Mechanical performances

In the study via the nanoscratch method, the lateral force can real-time feedback coating splitting by the diamond probe as it moves forward in real time [68]. On the directly coated pure Zn/PLGA surface, the mutation of lateral force was detected when the probe was loaded for about 3 s, indicating that the coating had partially peeled off, and the lateral force was about 25.5 mN at this time (Fig. S4(a)). When the probe was loaded for 6 s, the lateral force of the PDA-8.5/PLGA sample suddenly decreased, which was about 35.1 mN (Fig. S4(b)). When the scratch test was carried out on the surface of the PDA-10/PLGA sample, the tendency of lateral force curve on the surface was gentle, and only a slight change of lateral force was detected about 7.5 s after the experiment, where the lateral force was about 44.3 mN (Fig. S4(c)). Compared with pure Zn/PLGA, the level of lateral force and the smoothness and continuity of the lateral force-time curve were significantly improved in the samples coated with PDA, especially for PDA-10.

The vertical displacement-scratch distance curve after the scratch experiment was analyzed to evaluate the adhesion force more accurately. The more the steep displacement-distance curve fluctuates, the more serious the coating failure is [69]. The vertical displacement of the pure Zn/PLGA sample is the lowest, and the displacement mutation phenomenon is severe, corresponding to the lateral force mutation mentioned, proving that coating peel-off occurs (Fig. S4(d)). At this time, the vertical force is 80 mN. The curve of PDA-8.5/PLGA samples showed relatively more fluctuations, and many small displacement offsets were observed, while

the more considerable abrupt changes occurred at 113 mN probe pressure (Fig. S4(e)). The curve of PDA-10/PLGA samples maintained a nearly smooth trend proved the excellent adhesion of PDA-10 (Fig. S4(f)). In the 275 μm scratches distance, the vertical force was 141 mN, and the displacement offset mutation was detected. According to the above experimental results, PDA-10/PLGA samples showed a strong coating binding force

Using the advantages of high elongation of Zn, the surface morphology and fracture process of the film under different strains were analyzed by tensile test. In the case of 10% strain tensile, the coating fracture and peel were observed on the surface of pure Zn/PLGA. It demonstrates that the coating fracture starts from the bottom PLGA in direct contact with the Zn substrate and extends from the point to the surrounding, which is prone to extend in the horizontal direction perpendicular to the tensile direction. The surface coating of PDA-8.5/PLGA showed a slight cracking pattern but no evident coating rupture. The only slight fluctuation was observed on the surface of PDA-10/PLGA in some regions (Figs. S5 and 10(a)).

After 40% strain tensile, the lighter surface color of the pure Zn/PLGA indicates that the coating is thin, with localized cracking of the first and second layers, exposing the bottom layer and the Zn matrix. Transverse cracks appeared on the surface of PDA-8.5/PLGA, and some coatings cracked proved that the stepped morphology after corrosion can prevent the coating from being overstretched in the tensile direction, resulting in the deformation and cracking of the coating in the horizontal direction. Only fewer vertical cracks were observed in PDA-10/PLGA samples showing the superior strength of multilayer coating in stress loading. In ad-

dition, no significant large-scale coating shedding was observed (Figs. S6 and 10(b)).

In the fracture tensile case, the strain of the substrate is very great near the fracture region, even more than 60% in some areas. In this region of pure Zn/PLGA, the coating was torn in a wide range, directly exposing the Zn fracture morphology with only part of the bottom crimping PLGA film remaining, indicating that the film base connection was not firm. Due to the corrosion surface of PDA-8.5 would limit the film to be pulled apart parallelly to the tensile direction, small size cracks of the film were observed on the surface of PDA-8.5/PLGA. Compared with the previous sample, the density of damaged sites on the surface of the PDA-8.5/PLGA sample was higher. In contrast, in the PDA-10/PLGA samples near the fracture site, it was observed that the coating was still intact during the tensile process, but only some areas of the coating side appeared peeling (Figs. S7 and 10(c)).

4. Conclusion

In this work, we reported a surface modification strategy of biodegradable Zn via a one-step PDA coating method without introducing heavy metal elements or detrimental additives. In the PDA fabrication process under pH=10 condition, a dense ZnO passivation layer was formed to protect the Zn matrix from pitting corrosion under the improved deposition condition. Oxygen continuously brought by stirring participated in the reaction solution promptly to film the PDA coating with more than 6 times efficiency increased. The consecutive interface between Zn and PDA was successfully achieved by realizing the equilibrium between surface passivation and PDA polymerization. The smooth and pit-free coated structure possessed enhanced corrosion resistance nearly 30% than bare Zn and a desirable uniform corrosion mode illustrated by reducing local corrosion, corrosion products, and mass loss, which was beneficial for controllable degradation and inhibited deterioration of mechanical properties. The promise of anticoagulation was exhibited from PDA coated structure. And the PDA-10 performed much closer to normal range coagulation function. The superior anti-platelet adhesion property of coated Zn was confirmed with platelet adhesion decrease up to 40%, which could lower the risk of thrombosis. Thanks to the PDA coating on pure Zn, the uniform PLGA on the PDA double-coated Zn structure was fabricated. Superior mechanical performance of double-coated structure could be more stable and reliable in serving. It indicated that the application to couple the PDA coated Zn with multiple clinical treating needs, like drug loading. These results pave the way for active biodegradable metal surface modification and intervention instruments fabrication.

Declaration of Competing Interest

The authors declare that they have no known competing financial interests or personal relationships that could have appeared to influence the work reported in this paper.

Acknowledgments

This work was financially supported by the National Natural Science Foundation of China (No. 51975151), the Heilongjiang Provincial Natural Science Foundation of China (No. LH2019E041), and the Heilongjiang Touyan Innovation Team Program.

Supplementary materials

Supplementary material associated with this article can be found, in the online version, at doi:10.1016/j.jmst.2021.12.076.

References

- [1] M. Li, X. Xu, Z. Jia, Y. Shi, Y. Cheng, Y. Zheng, *J. Mater. Chem. B* 5 (2017) 1182–1194.
- [2] C. Shuai, S. Li, S. Peng, P. Feng, Y. Lai, C. Gao, *Mater. Chem. Front.* 3 (2019) 544–562.
- [3] C. Wang, H. Fang, X. Qi, C. Hang, Y. Sun, Z. Peng, W. Wei, Y. Wang, *Acta Biomater.* 91 (2019) 99–111.
- [4] H. Li, P. Wang, G. Lin, J. Huang, *Acta Biomater.* 129 (2021) 33–42.
- [5] G. Guagliumi, A. Farb, G. Musumeci, O. Valsecchi, M. Tespili, T. Motta, R. Virmani, *Circulation* 107 (2003) 1340–1341.
- [6] M. Peuster, C. Hesse, T. Schloo, C. Fink, P. Beerbaum, C. von Schnakenburg, *Biomaterials* 27 (2006) 4955–4962.
- [7] R. Walkman, R. Pakala, R. Baffour, R. Seabron, D. Hellings, F.O. Tio, *J. Interv. Cardiol.* 21 (2008) 15–20.
- [8] D. Pierson, J. Edick, A. Tauscher, E. Pokorney, P. Bowen, J. Gelbaugh, J. Stinson, H. Getty, C.H. Lee, J. Drelich, J. Goldman, *J. Biomed. Mater. Res. Part B* 100B (2012) 58–67.
- [9] Z.A. Ali, P.W. Serruys, T. Kimura, R. Gao, S.G. Ellis, D.J. Kereiakes, Y. Onuma, C. Simonton, Z. Zhang, G.W. Stone, *Lancet* 390 (2017) 760–772.
- [10] J. Shi, X. Miao, H. Fu, A. Jiang, Y. Liu, X. Shi, D. Zhang, Z. Wang, *Biometals* 33 (2020) 217–228.
- [11] K. Hanada, K. Matsuzaki, X. Huang, Y. Chino, *Mater. Sci. Eng. C* 33 (2013) 4746–4750.
- [12] Q. Ge, D. Dellasega, A.G. Demir, M. Vedani, *Acta Biomater.* 9 (2013) 8604–8610.
- [13] J. Liu, B. Zheng, P. Wang, X. Wang, B. Zhang, Q. Shi, T. Xi, M. Chen, S. Guan, *ACS Appl. Mater. Interfaces* 8 (2016) 17842–17858.
- [14] A. Atrens, S. Johnston, Z. Shi, M.S. Dargusch, *Scr. Mater.* 154 (2018) 92–100.
- [15] A. Atrens, Z. Shi, S.U. Mehreen, S. Johnston, G.L. Song, X. Chen, F. Pan, *J. Magn. Alloy.* 8 (2020) 989–998.
- [16] Chemistry LibreTexts, 6.2: Standard Electrode Potentials, https://chem.libretexts.org/Courses/Mount_Royal_University/Chem_1202/Unit_6%253A_Electrochemistry/6.2%253A_Standard_Electrode_Potentials, May 9, 2021.
- [17] S.A. Read, S. Obeid, C. Ahlenstiel, G. Ahlenstiel, *Adv. Nutr.* 10 (2019) 696–710.
- [18] P.K. Bowen, J. Drelich, J. Goldman, *Adv. Mater.* 25 (2013) 2577–2582.
- [19] H. Hermawan, D. Dubé, D. Mantovani, *Acta Biomater.* 6 (2010) 1693–1697.
- [20] B. Hiebl, E. Nennig, S. Schiestel, A. Kovacs, F. Jung, H. Fischer, *Clin. Hemorheol. Microcirc.* 61 (2015) 205–211.
- [21] P.K. Bowen, R.J. Guillory, E.R. Shearier, J.M. Seitz, J. Drelich, M. Bocks, F. Zhao, J. Goldman, *Mater. Sci. Eng. C* 56 (2015) 467–472.
- [22] E. Mostaed, M. Sikora-Jasinska, J.W. Drelich, M. Vedani, *Acta Biomater.* 71 (2018) 1–23.
- [23] J. Cheng, B. Liu, Y.H. Wu, Y.F. Zheng, *J. Mater. Sci. Technol.* 29 (2013) 619–627.
- [24] Z. Li, Z.Z. Shi, Y. Yan, D. Zhang, K. Yang, H.F. Li, H. Zhang, L.N. Wang, *Corros. Sci.* 189 (2021) 109564.
- [25] J. Ma, N. Zhao, D. Zhu, *Sci. Rep.* 6 (2016) 1–10.
- [26] K. Beaussant Törne, A. Örnberg, J. Weissenrieder, *Electrochim. Acta* 258 (2017) 1476–1483.
- [27] L. Liu, Y. Meng, C. Dong, Y. Yan, A.A. Volinsky, L.N. Wang, *J. Mater. Sci. Technol.* 34 (2018) 2271–2282.
- [28] L. Liu, Y. Meng, A.A. Volinsky, H.J. Zhang, L.N. Wang, *Corros. Sci.* 153 (2019) 341–356.
- [29] E.R. Shearier, P.K. Bowen, W. He, A. Drelich, J. Drelich, J. Goldman, F. Zhao, *ACS Biomater. Sci. Eng.* 2 (2016) 634–642.
- [30] S. Agarwal, J. Curtin, B. Duffy, S. Jaiswal, *Mater. Sci. Eng. C* 68 (2016) 948–963.
- [31] Z.Z. Yin, W.C. Qi, R.C. Zeng, X.B. Chen, C.D. Gu, S.K. Guan, Y.F. Zheng, *J. Magn. Alloy.* 8 (2020) 42–65.
- [32] W. Yuan, D. Xia, S. Wu, Y. Zheng, Z. Guan, J.V. Rau, *Bioact. Mater.* 7 (2022) 192–216.
- [33] H. Lee, S.M. Dellatore, W.M. Miller, P.B. Messersmith, *Science* 318 (2007) 426–430.
- [34] F. Singer, M. Schlesak, C. Mebert, S. Höhn, S. Virtanen, *ACS Appl. Mater. Interfaces* 7 (2015) 26758–26766.
- [35] Y. Chen, S. Zhao, M. Chen, W. Zhang, J. Mao, Y. Zhao, M.F. Maitz, N. Huang, G. Wan, *Corros. Sci.* 96 (2015) 67–73.
- [36] L. Chen, J. Li, S. Wang, S. Zhu, C. Zhu, B. Zheng, G. Yang, S. Guan, *J. Mater. Res.* 33 (2018) 4123–4133.
- [37] X. Liu, Z. Chen, J. Liu, T. Xi, Y. Zheng, S. Guan, Y. Zheng, Y. Cheng, *J. Mater. Sci. Technol.* 31 (2015) 733–743.
- [38] P. Wang, P. Xiong, J. Liu, S. Gao, T. Xi, Y. Cheng, *J. Mater. Chem B* 6 (2018) 966–978.
- [39] J. Li, L. Chen, X. Zhang, S. Guan, *Mater. Sci. Eng. C* 109 (2020) 110607.
- [40] Q. Wei, F. Zhang, J. Li, B. Li, C. Zhao, *Polym. Chem.* 1 (2010) 1430–1433.
- [41] C. Zhang, Y. Ou, W.X. Lei, L.S. Wan, J. Ji, Z.K. Xu, *Angew. Chem. Int. Ed.* 55 (2016) 3054–3057.
- [42] G.J. Brewer, *Chem. Res. Toxicol.* 23 (2010) 319–326.
- [43] S. Hong, Y.S. Na, S. Choi, I.T. Song, W.Y. Kim, H. Lee, *Adv. Funct. Mater.* 22 (2012) 4711–4717.
- [44] Y. Ding, L.T. Weng, M. Yang, Z. Yang, X. Lu, N. Huang, Y. Leng, *Langmuir* 30 (2014) 12258–12269.
- [45] J.H. Ryu, P.B. Messersmith, H. Lee, *ACS Appl. Mater. Interfaces* 10 (2018) 7523–7540.
- [46] Z. Yang, X. Zhao, R. Hao, Q. Tu, X. Tian, Y. Xiao, K. Xiong, M. Wang, Y. Feng, N. Huang, G. Pan, *PNAS* 117 (2020) 16127–16137.
- [47] X. Wang, S.S. Venkatraman, F.Y.C. Boey, J.S.C. Loo, L.P. Tan, *Biomaterials* 27 (2006) 5588–5595.

- [48] J. Liu, T. Xi, J. Mater. Sci. Technol. 32 (2016) 845–857.
- [49] C. Martins, F. Sousa, F. Araújo, B. Sarmento, Adv. Healthc. Mater. 7 (2018) 1701035.
- [50] X. Du, L. Li, J. Li, C. Yang, N. Frenkel, A. Welle, S. Heissler, A. Nefedov, M. Grunze, P.A. Levkin, Adv. Mater. 26 (2014) 8029–8033.
- [51] W. Wu, Z. Liu, Q. Wang, X. Li, Corros. Sci. 170 (2020) 108693.
- [52] W. Wu, X. Cheng, J. Zhao, X. Li, Corros. Sci. 165 (2020) 108416.
- [53] J. Li, L. Tan, X. Liu, Z. Cui, X. Yang, K.W.K. Yeung, P.K. Chu, S. Wu, ACS Nano 11 (2017) 11250–11263.
- [54] N. Yang, T. Yang, W. Wang, H. Chen, W. Li, J. Hazard. Mater. 377 (2019) 142–151.
- [55] G. Zhang, X. Zhang, Y. Yang, R. Chi, J. Shi, R. Hang, X. Huang, X. Yao, P.K. Chu, X. Zhang, Biomater. Sci. 8 (2019) 391–404.
- [56] S.H. Ku, J.S. Lee, C.B. Park, Langmuir 26 (2010) 15104–15108.
- [57] S.A. Centeno, J. Shamir, J. Mol. Struct. 873 (2008) 149–159.
- [58] Z. Xia, G. Liu, Y. Dong, Y. Zhang, Prog. Org. Coat. 133 (2019) 154–160.
- [59] A. Davydov, Molecular Spectroscopy of Oxide Catalyst Surfaces, John Wiley & Sons, New Jersey, 2003.
- [60] X. Liu, W. Yuan, D. Shen, Y. Cheng, D. Chen, Y. Zheng, Corros. Sci. 189 (2021) 109606.
- [61] S. Huang, L. Chen, B. Jiang, L. Qiao, Y. Yan, J. Electroanal. Chem. 886 (2021) 115145.
- [62] S. Huang, W. Wu, Y. Su, L. Qiao, Y. Yan, Corros. Sci. 178 (2021) 109071.
- [63] G. Totea, D. Ionita, I. Demetrescu, M. Mitache, Open Chem. 12 (2014) 796–803.
- [64] R. Yang, L. Moosavi, Prothrombin Time, <http://www.ncbi.nlm.nih.gov/books/NBK544269/>, May 10, 2021.
- [65] Clinical Laboratory Science, Activated Partial Thromboplastin Time (APTT), <https://clinicalsci.info/activated-partial-thromboplastin-time-aptt/>, May 5, 2020.
- [66] R. Vilar, R.J. Fish, A. Casini, M. Neerman-Arbez, Haematologica 105 (2020) 284–296.
- [67] T. Groth, E.J. Campbell, K. Herrmann, B. Seifert, Biomaterials 16 (1995) 1009–1015.
- [68] D.X. Han, G. Wang, J.L. Ren, L.P. Yu, J. Yi, I. Hussain, S.X. Song, H. Xu, K.C. Chan, P.K. Liaw, Acta Mater. 136 (2017) 49–60.
- [69] X. Wang, P. Xu, R. Han, J. Ren, L. Li, N. Han, F. Xing, J. Zhu, Nanotechnol. Rev. 8 (2019) 628–644.